CHAPTER 2 HIGH THROUGHPUT CHARACTERIZATION OF $(La_{0.8}Sr_{0.2})_{0.95}MnO_{3+\delta}$ THIN FILM MICROELECTRODES

This chapter introduces the scanning impedance probe, a robotic instrument that can rapidly measure the electrochemical impedance response of hundreds of thin film electrodes in automated fashion. This instrument is combined with a parallel fabrication method that produces libraries containing hundreds of thin film electrodes with systematically varied properties on a single substrate. Results are presented from libraries of $(La_{0.8}Sr_{0.2})_{0.95}MnO_{3+\delta}$ (LSM) microelectrodes with systematically varied area, thickness, and growth temperature. The measured impedance spectra are well fit by a physically derived electrochemical model, and all trends are consistent with a pathway involving oxygen reduction over the entire surface of the LSM microelectrode followed by diffusion through the film and into the YSZ electrolyte. The surface activity is found to be correlated with the number of exposed grain boundary sites, suggesting that grain boundaries are more active than grains towards the rate-limiting surface process.

2.1 Introduction

As described in Chapter 1, in recent years many studies have probed patterned thin film electrodes using electrochemical impedance spectroscopy to yield rich insights into the behavior of mixed ionic and electronic conductors (MIECs), including accurate measurements of the intrinsic surface activity of such materials towards oxygen electro-reduction.[5] This chapter builds on the success of the patterned thin film electrode approach by adding two innovations that increase throughput and reliability. First, a scanning impedance probe is described that can perform data acquisition and processing with higher throughput. Second, libraries of thin film microelectrodes with systematically varied film thickness or growth temperature are fabricated and characterized on a single solid electrolyte substrate. This parallel fabrication method helps to further improve throughput, and it helps avoid unintended differences that can arise when samples are prepared or measured in series. Such differences can mask trends with the parameters of interest.

In the specific case of $(La_{1-x}Sr_x)_{1-y}MnO_{3+\delta}$, a heavily studied cathode material that is commonly used in commercial applications,[2,3] both patterned and unpatterned thin film studies have reached agreement that the three phase boundary pathway, wherein oxygen incorporation into the electrolyte occurs at the boundary of the LSM, electrolyte, and gas phases, is not always dominant, but can be outcompeted by a through-the-film pathway, wherein oxygen ions incorporate at the LSM surface, diffuse through the LSM film, and then cross into the electrolyte.[9,10,19,20] Moreover, the shapes of the impedance spectra reported in these studies are broadly similar; the typical spectrum includes a high frequency feature that exhibits relatively little change with film thickness, and a low frequency semicircle with a characteristic resistance that scales approximately linearly with increasing film thickness.

However, there is substantial disagreement in the interpretation of these spectra and in the conclusions drawn about the rates of the surface and bulk steps. In light of the thickness trends just described, several studies suggested that the high-frequency feature corresponds to the surface incorporation process, and that the low frequency semicircle corresponds to bulk diffusion through the film.[20-22] However, these reports do not mention the possibility that surface properties (like the number of exposed grain boundaries) may depend on thickness.

On the other hand, using fits by an equivalent circuit based on a physically derived model for MIECs, Fleig et al. assigned the high frequency feature to bulk diffusion and the low frequency semicircle to surface incorporation.[10] These authors noted that the resulting surface exchange rate increased somewhat with increasing thickness, and they commented that there may be a "thickness-dependent film structure and chemistry".

The present study seeks to resolve this disagreement, which is important because of its direct implications for how to improve surface activity in an LSM-based cathode. In particular, if the largest contribution to the electrode resistance comes from surface incorporation, then modifying the LSM surface (e.g., by decoration with catalyst particles) could be a fruitful strategy. In contrast, if the largest resistance contribution comes from diffusion through the film, then alternate strategies would be more beneficial.

2.2 Overview of the scanning impedance probe

The configuration of the scanning impedance probe is shown schematically in Figure 2.1 and to scale in Figure S17.

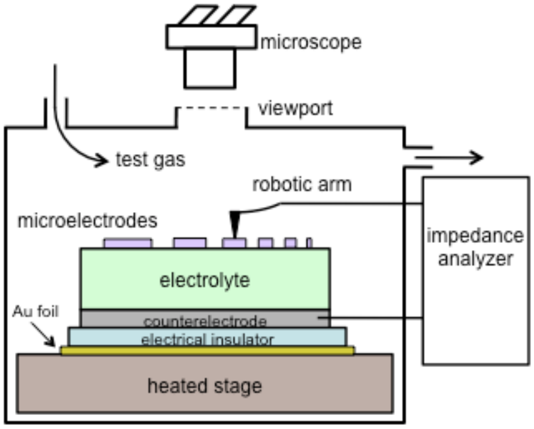

Figure 2.1. Schematic of the test configuration in the scanning impedance probe. Dimensions are not to scale.

Compared to previously reported instruments for probing microelectrodes,[9,23] the most significant new feature here is the scanning capability: the position of the alumina arm holding the metal probe tip is determined by three orthogonal lead screws connected to stepper motors (Figure S17). Thus the metal probe tip can be touched to a microelectrode simply by entering the coordinates of that microelectrode in the control software. The temperature and gas environment are also controlled in software. Moreover, the dimensional tolerances associated with the patterning process are small enough that the relative spacing of the microelectrodes on the substrate surface can be accurately predicted, and three points are sufficient to define the plane of that surface. Consequently, once the user manually finds the coordinates of three reference microelectrodes in a library, the coordinates of all the other microelectrodes can be readily computed. Hundreds of microelectrodes can then be probed in any desired sequence over a range of environmental conditions in automated fashion.

2.3 Experimental procedures

A sintered pellet of $(La_{0.8}Sr_{0.2})_{0.95}MnO_3$ (LSM) was prepared for use as a pulsed laser deposition target as follows. First, a dense compact was prepared from 20 g commercial powder (Fuel Cell Materials, 99.5% pure) with 1 wt% polyvinylpyrrolidone added to serve as a binder. The powder was subjected to uniaxial pressure under 20 MPa for 10 min in a 32 mm diameter die, followed by isostatic pressure under 350 MPa for 20 min. The edges and faces of this powder compact were shaved using a razor to remove any surface contamination from the die, then this powder compact was placed on an alumina support with excess powder spread below the compact to avoid reactivity with the alumina. The compact was then sintered at 1450 ˚C for 5 h in stagnant air in a dedicated alumina tube. The resulting pellet was polished on all sides with sandpaper down to 600 grit, sonicated in water and isopropanol to remove the residual grit, and finally measured as having 26 mm diameter and 6 mm thickness. X-ray diffraction (XRD, Philips X'Pert Pro, Cu Ka) patterns acquired from both faces of the pellet showed good agreement with patterns reported in the Inorganic Crystal Structure Database for a virtually identical composition ($La_{0.8}Sr_{0.2}MnO_3$).

Using this target, $(La_{0.8}Sr_{0.2})_{0.95}MnO_3$ films were grown on (100)-oriented single crystal $Y_{0.15}Zr_{1.85}O_{1.93}$ substrates (YSZ, 8 mol% Y_2O_3-stabilized ZrO_2, 5 mm x 10 mm x 0.5 mm, MTI Corporation) by pulsed laser deposition with a KrF excimer laser (248 nm, 0.8 J/cm^2, 1 Hz). During film growth, each substrate was adhered to a heated stage with silver paste, which was subsequently scraped off.

On two substrates, the *thickness* of the LSM film was systematically varied by using a motor to slowly draw an Inconel shutter across the deposition plume during growth. This procedure created two "thickness libraries" in which the film thickness varied continuously from 30 nm to 300 nm across the substrate. The deposition parameters for Library #1 were as follows: 650 ˚C growth temperature, 10 mtorr O_2 working pressure, 1 Hz ablation laser pulse frequency, 0.7 nm/min deposition rate, and 100 ˚C/min cooling rate. For Library #2, all conditions were identical with the exception of the working pressure, which was held at 30 mtorr O2.

On a third substrate, the *growth temperature* of the LSM film was systematically varied using an asymmetric stage geometry (shown in Figure S18) heated at one end with infrared radiation. This procedure created a "growth temperature library", Library #3, in which the growth temperature varied continuously from 555 ˚C to 725 ˚C across the substrate. The substrate temperature was measured in numerous places during growth using an optical pyrometer. Other deposition parameters for Library #3 were as follows: uniform 135 nm thickness, 30 mtorr O_2 pressure, 5 Hz ablation laser pulse frequency, 2.7 nm/min deposition rate (calibrated in advance by acquiring atomic force microscopy (AFM, Digital Instruments Nanoscope III) profiles from test films prepared with the same target and deposition parameters), and 20 ˚C/min cooling rate.

After growth, XRD patterns, rocking curves, and AFM micrographs were acquired from each film in several regions (Bruker D8 Discover, Cu $K\alpha$). Each film was then patterned into a library of microelectrodes using photolithography and ion milling. Specifically, two coats of photoresist (Shipley 1813) were applied by spin coating on top of each film, exposure to UV radiation through a photomask, and then development. The film then underwent ion milling for 45 min resulting in a milling depth of ~350 nm. The residual photoresist was then chemically stripped. In this way, each film was converted into a library of 337 circular microelectrodes. Each library included nine different values of microelectrode diameter spanning the range 50 μm - 500 μm. The "growth temperature library" included twenty-one different values of growth temperature, unevenly spaced from 555 ˚C - 725 ˚C, while the thickness libraries included twenty-one different values of film thickness, evenly spaced from 30 nm - 300 nm. Because the thickness or growth temperature varied continuously across each library it also varied slightly across each microelectrode. However, the microelectrodes had small enough diameter that a single value of thickness or growth temperature (the local average value) could be assigned to each microelectrode with minimal loss of accuracy. Specifically, for Libraries #1 and #2 the difference in thickness across the largest microelectrode probed (500 μm) is 15 nm, while for Library #3 the difference in growth temperature across the largest microelectrode probed (200 μm) was ~ 5 ˚C.

After patterning the libraries were characterized by optical microscopy and again by AFM. In preparation for impedance measurements, each substrate was then adhered to a ~ 10 mm x 20 mm x 0.6 mm alumina sheet using silver paste (DAD-87, Shanghai Research Institute). Heat treatment in a quartz tube under stagnant air at 600 ˚C - 700 ˚C for 1 h induced sintering of the paste into a porous counter electrode.

Thus prepared, Library #1 was installed in the scanning impedance probe and heated to a stage temperature of 750 ˚C, which corresponded to a microelectrode temperature during probing of ~710 ˚C. A more detailed discussion of the temperature calibration is given in the Supplemental Information. The oxygen partial pressure (pO2) in the chamber was varied over the range 10^{-3} atm - 1 atm by flowing bottled oxygen or oxygen-nitrogen mixtures through the chamber and then past a zirconia-based oxygen sensor (Setnag) housed in a quartz tube in a separate furnace. The pO2 was allowed to stabilize at each condition prior to the acquisition of impedance measurements; typical stabilization times were 0.5 h - 3 h. The total pressure in the chamber was always 1 atm. The microelectrodes were contacted using a probe tip made of Paliney7, a commercial alloy containing 35% Pd, 30% Ag, 14% Cu, 10% Au, 10% Pt, 1% Zn (American Probe & Technologies, 20 μm tip radius). Several measurements were repeated using a probe tip made of $Pt_{0.7}Ir_{0.3}$ (Moser, 10 μm tip radius); identical impedance results were obtained. The former probe material was preferred because it did not scratch the microelectrodes.

Impedance spectra were acquired using a frequency response analyzer (Solartron Modulab) with an applied a.c. voltage of 30 mV, no applied d.c. bias, and a typical frequency range of 10 kHz - 16 mHz. As described in the Supplemental Information, cooling of the sample by the probe tip generated a temperature drop between the electrodes that has an associated 5 mV - 25 mV Seebeck voltage (with the exact value depending on the microelectrode diameter (Figure S19)), so in fact each impedance spectrum was effectively measured under 5 mV - 25 mV anodic d.c. bias, which was verified to be negligibly small for this material system. The analyzer calibration was verified in advance by acquiring impedance spectra from test circuits containing precision megaohm resistors and nanofarad capacitors; fits to these spectra reproduced the resistance and capacitance values with < 3% error. Impedance spectra acquired from the LSM microelectrodes were fit by an expression first suggested by Fleig et al.[10] and described in detail below.

Morphological features were reexamined after impedance measurements. The sample surfaces were coated with a conductive layer of ~ 10 nm carbon (Cressington 108) and/or ~ 10 nm osmium and then characterized by scanning electron microscopy (SEM, Zeiss 1550 VP) and energy dispersive spectroscopy (EDS, Oxford X-Max SDD). Additionally, a protective layer of several hundred nm platinum was deposited in a few regions of each sample, and then cross-sections of these regions were prepared and imaged using focused ion beam (FIB) milling and SEM (FEI Helios Nanolab 600). The libraries were then characterized by optical profiling (New View 6000).

2.4 Results of Physical Characterization

X-ray diffraction patterns acquired after growth and prior to patterning are shown below. Figure 2.2a and Figure S20 show the results from the thickness libraries, Libraries #1 and #2. The patterns exhibit reflections that correspond primarily to (110)-oriented grains. Some intensity from (012) or (202) reflections is also evident. Figure 2.2b corresponds to Library #3, the growth temperature library. At growth temperatures of ~580 ˚C and lower, the XRD patterns show no reflections from the film, indicating those regions of the film are mostly amorphous. The possibility of slower film growth at those temperatures was ruled out by subsequent optical profiling, which indicated the film thickness was uniform throughout the sample. Moreover, the film color appeared uniform across the sample by visual inspection, consistent with a uniform thickness, whereas in other samples, decreased thickness gave rise to a lighter color. At growth temperatures of ~615 ˚C and higher, the films appear crystalline with similar orientations as measured from the thickness library.

Rocking curves obtained from Library #3 were best fit using two Voigt peaks, yielding two sets of FWHM values (Figure S21) and suggesting that the films had a thin epitaxial layer adjacent to the substrate and a thicker non-epitaxial layer elsewhere.

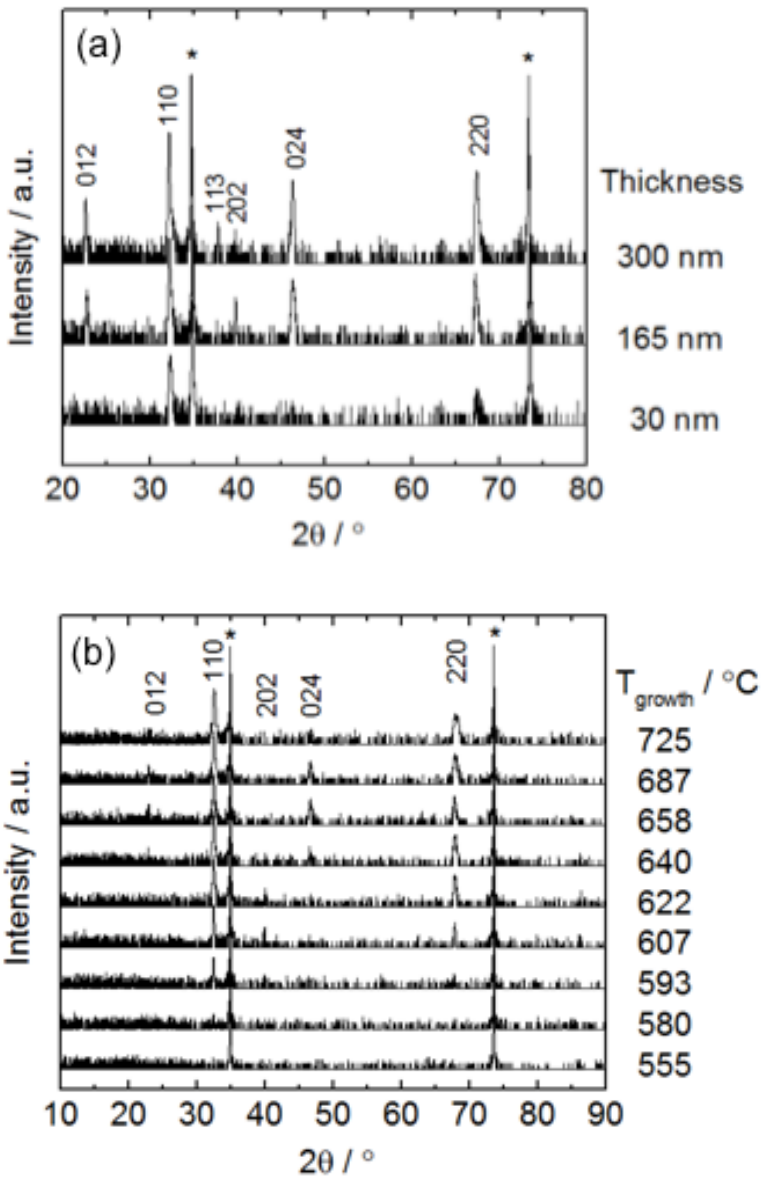

Figure 2.2. X-ray diffraction patterns acquired from various regions of two $(La_{0.8}Sr_{0.2})_{0.95}MnO_{3+\delta}$ thin film libraries: (a) Library #1, 30 - 300 nm thickness, 650 ˚C growth temperature, 10 mtorr O_2 growth pressure, 1 Hz laser pulse rate. (b) Library #3, 135 nm thickness, 555 - 725 ˚C growth temperature, 30 mtorr O_2 growth pressure, 5 Hz laser pulse rate. The orientation of each LSM reflection is indicated. Reflections marked with an asterisk are from the YSZ substrate.

After patterning each film, the layout shown in Figure 2.3 was obtained. The microelectrode diameters were measured by digital optical microscopy and found to be within 5% of the nominal diameters. As the microelectrode thickness increases from 30 nm to 150 nm, the microelectrodes become discernibly darker in color. Thickness increases past 150 nm are not discernible by eye. This effect is visible in Figure 2.3.

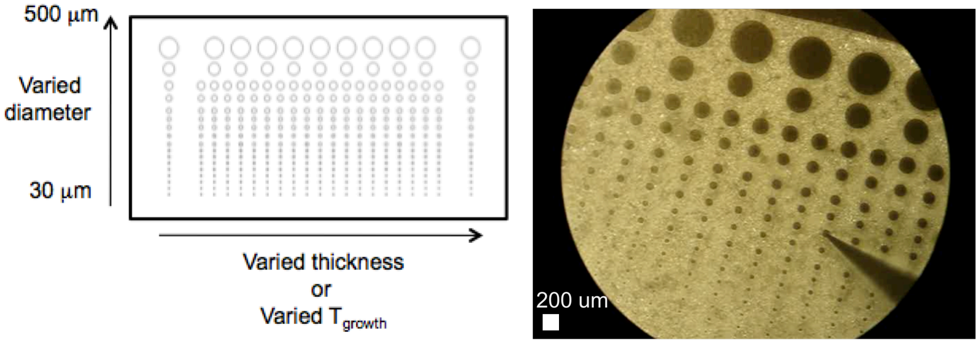

Figure 2.3. Typical library of $(La_{0.8}Sr_{0.2})_{0.95}MnO_{3+\delta}$ thin film microelectrodes grown on a 5 mm x 10 mm $Y_{0.15}Zr_{1.85}O_{1.93}$ substrate. Left: schematic layout. Right: optical photo of Library #1 during impedance measurements.

The microelectrode surfaces were characterized by AFM before and after patterning. No changes were observed due to the patterning. Micrographs taken after patterning are shown in Figure 2.4 and Figure S22 (for Libraries #1 and #2) and in Figure 2.5 (for Library #3). The grain size is seen to increase with increasing thickness (Figure 2.4 and Figure S22) or increasing growth temperature (Figure

2.5). Equivalently, the area density of exposed grain boundary length decreases with either increasing growth temperature or increasing thickness. These trends are consistent with findings from previous studies of oxide film growth.[24,25]

Importantly, these grain size differences persisted throughout the impedance experiments. For example, the smaller grain sizes obtained from growth at 555 ˚C were retained even after days of subsequent annealing at 710 ˚C (Figure S23). This finding has two important implications. First, cation mobility is evidently faster during film growth at a certain temperature (in 10 mtorr O_2) than during subsequent anneals at the same temperature (in 1 torr O_2 - 760 torr O_2). Second, the thickness libraries and growth temperature library prepared in this work were also effectively "grain size libraries" with grain sizes that remained stable during the electrochemical impedance measurements.

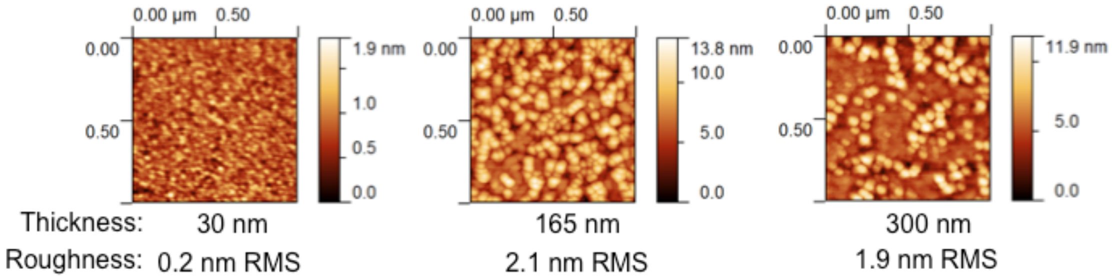

Figure 2.4. Atomic force micrographs acquired after patterning from a thickness library of $(La_{0.8}Sr_{0.2})_{0.95}MnO_{3+\delta}$ microelectrodes (Library #1, uniform 650 ˚C growth temperature). The corresponding thickness and root-mean-squared roughness are listed under each micrograph.

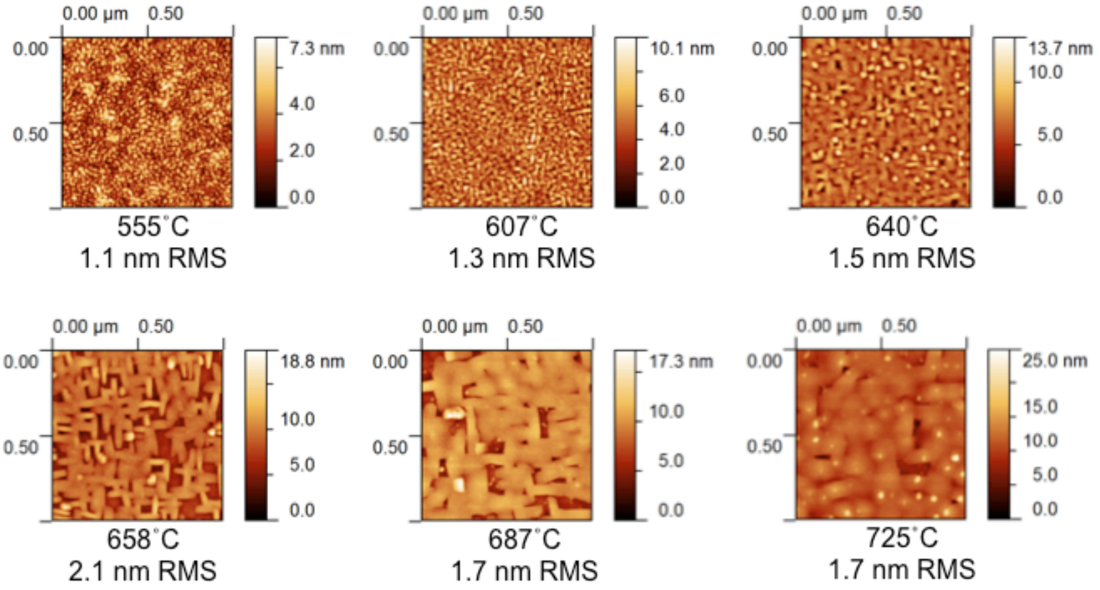

555˚C
1.1 nm RMS

607˚C
1.3 nm RMS

640˚C
1.5 nm RMS

658˚C
2.1 nm RMS

687˚C
1.7 nm RMS

725˚C
1.7 nm RMS

Figure 2.5. Atomic force micrographs acquired after patterning from a growth temperature library of $(La_{0.8}Sr_{0.2})_{0.95}MnO_{3+\delta}$ microelectrodes (Library #3, uniform 135 nm thickness). The corresponding growth temperature and root-mean-squared roughness are listed under each micrograph.

Cross-sectional FIB-SEM images (acquired after impedance testing from multiple regions in the libraries) indicated that the films were dense. A representative image is shown in Figure 2.6.

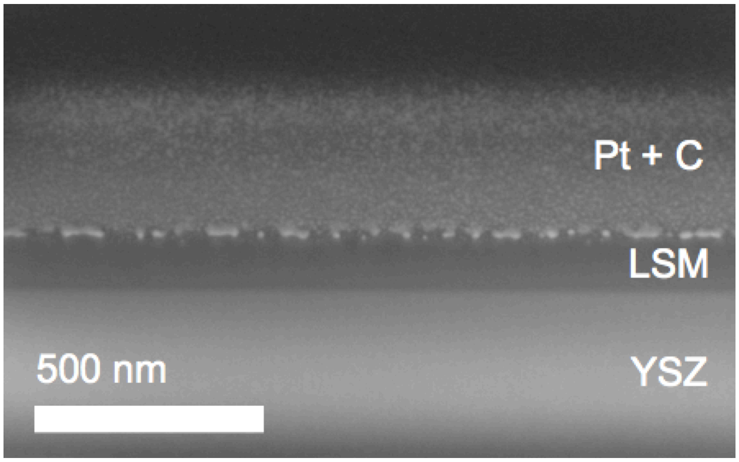

Figure 2.6. FIB-SEM cross-section acquired from a growth temperature library of $(La_{0.8}Sr_{0.2})_{0.95}MnO_{3+\delta}$ films (Library #3) after impedance testing. The sample was coated with conductive and protective layers of carbon and platinum prior to FIB milling to facilitate imaging. This image was acquired using a tilt angle of 52° off normal.

2.5 Results of Electrochemical Characterization

The reaction pathway posited in this study is shown in Figure 2.7. This pathway involves oxygen electro-reduction over the entire surface of the film, followed by ion diffusion through the film and into the electrolyte substrate.

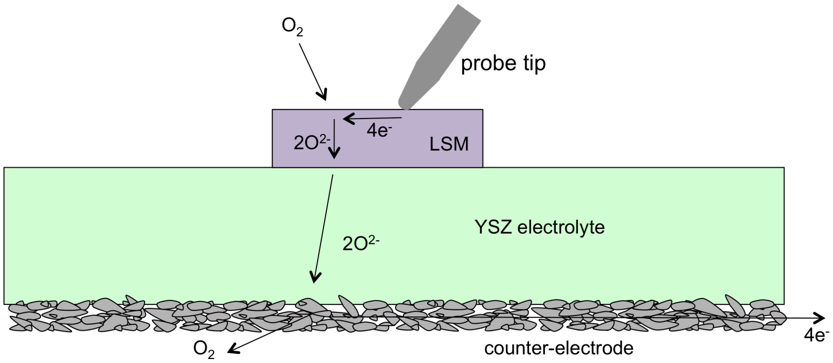

Figure 2.7. Schematic of a through-the-film reaction pathway.

It has been shown elsewhere that the electrochemical impedance response arising from 1D diffusion through a mixed ionic and electronic conductor (MIEC) can be rigorously mapped to an equivalent circuit based on a generalized transmission model.[26,27] Here that result is modified to apply to the configuration in Figure 2.7 as follows: the LSM microelectrode film is treated as a MIEC; the resistance to bulk electron migration normal to the substrate is neglected in recognition of the high electronic conductivity of LSM; the LSM/YSZ interface is assumed to be reversible to ions and blocking to electrons, and thus is modeled by a simple (double-layer) electronic capacitance; and an additional resistance is added in series to account for bulk ion diffusion through the YSZ electrolyte and lateral electron migration (sheet resistance) from the probe tip to the surface reaction sites. Additionally, the impedance arcs measured at the lower frequencies in this study were consistently observed to be depressed relative to ideal semi-circles, suggesting a dispersion of time constants; this dispersion was accounted for by replacing the surface ionic capacitance with a constant phase element.

With these modifications in hand, the effective equivalent circuit is shown in Figure 2.8. This circuit is virtually identical to the one presented previously by Fleig et al.,[10] except in that study a constant phase element was substituted for the interfacial electronic capacitance rather than the surface ionic capacitance. In the current study, that alternative circuit yielded poorer fits and unreasonably large confidence intervals.

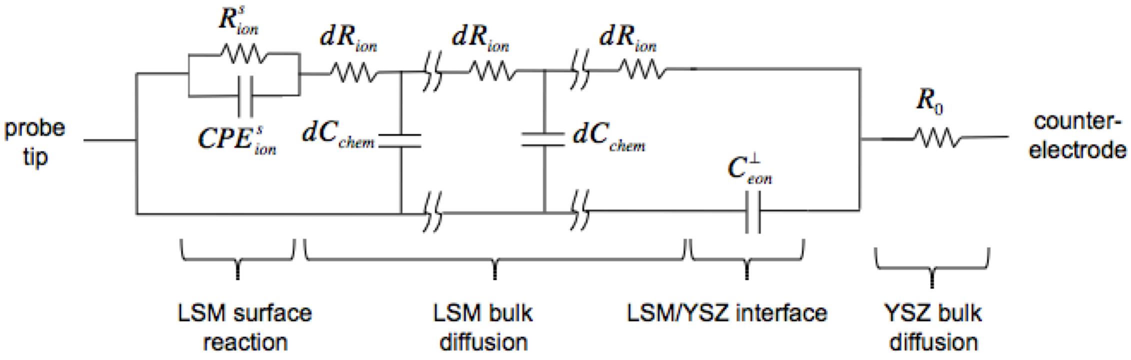

Figure 2.8. Equivalent circuit corresponding to the reaction pathway shown in Figure 2.7.

An analytical expression for the complex impedance of the equivalent circuit in Figure 2.8 can be derived using Kirchhoff's Laws, as described previously.[9] The result is:

$$Z = \frac{Z_1 Z_D + Z_D Z_A a \cdot \coth(a)}{Z_1 + Z_A Z_D a^2 / Z_1 + (Z_A + Z_D) a \cdot \coth(a)} + R_0 \qquad (1)$$

where $Z_1 = R_{ion}$, $Z_D = \frac{1}{jwC_{eon}^{\perp}}$, $Z_A = \frac{R_{ion}^s}{1 + R_{ion}^s Y_{ion}^s (jw)^n}$, $a = \sqrt{jwR_{ion}C_{chem}}$, w is the radial frequency, and $j = \sqrt{-1}$. The seven fit parameters in this model are R_{ion}^s, Y_{ion}^s, n, R_{ion}, C_{chem}, C_{eon}, and R_0, which correspond to the LSM surface exchange resistance, the LSM surface ionic capacitance (in the form of a constant phase element magnitude and exponent), the LSM through-film oxygen ion diffusion resistance, the LSM chemical capacitance, the LSM/YSZ interfacial electronic capacitance, and the YSZ oxygen ion diffusion resistance. The other variables (Z_1, Z_D, Z_A, and a) are merely placeholders that facilitate algebraic manipulations. After fitting, the effective surface ionic capacitance C_{ion}^s was calculated from the standard expression $C_{ion}^s = (Y_{ion}^s)^{1/n} R^{(1/n)-1}$. The data were fit by Equation 1 using complex nonlinear least squares, implemented in a custom Matlab routine. In the fitting routine, the residual of each complex impedance datum was weighted by the complex modulus of the datum. The initial values for the fit parameters were selected as described in the Supplemental Information.

Raw impedance spectra and the corresponding fit curves from a thickness library, Library #1, are shown in Figure 2.9. In the complex-plane plot, a large arc is observed at lower frequencies, and an additional smaller feature is observed at higher frequencies. These spectra appear quite similar to those observed by Fleig et al.[10], and they are broadly similar to the spectra observed in other reports as well.[20-22] Note that at lower oxygen pressures, the two features are more distinct, while at higher oxygen pressures they begin to merge. Additional spectra and fits from Library #1 are shown in Figure 2.10 as a function of film thickness. The low frequency arc clearly grows with increasing thickness, as observed by previous workers.

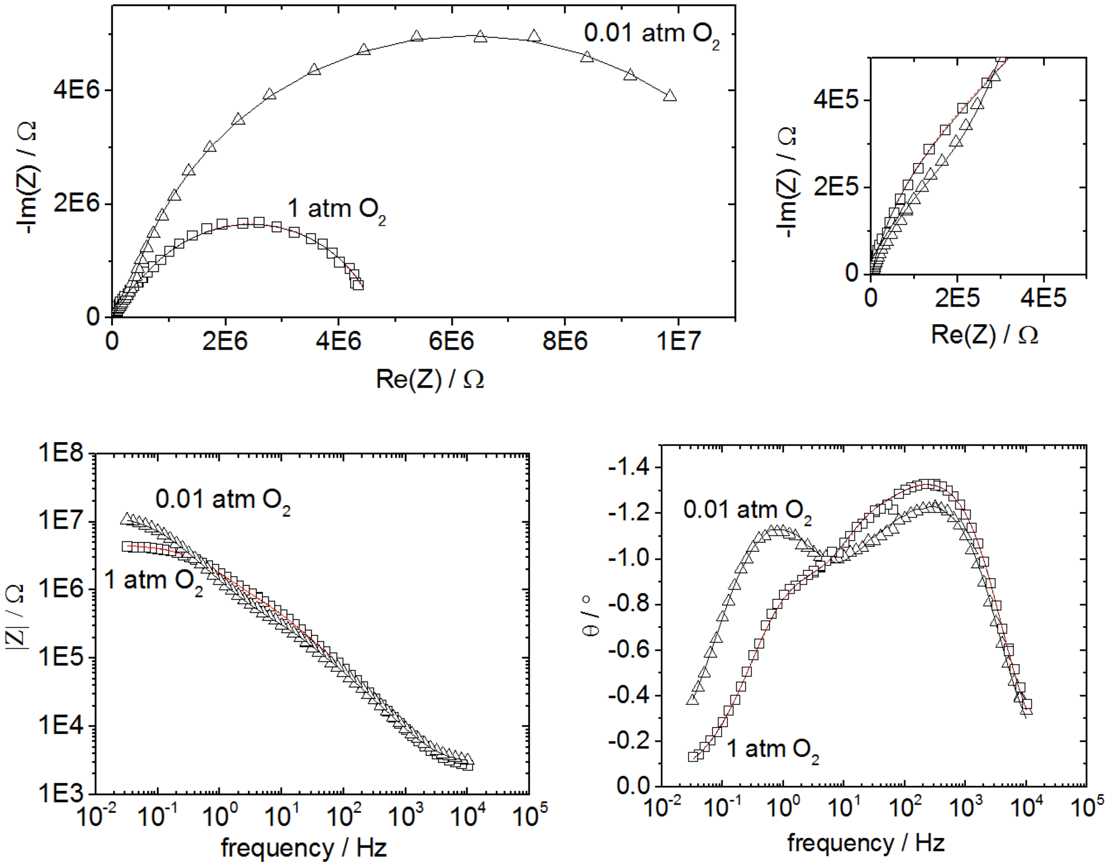

Figure 2.9. Typical impedance spectra (a), zoomed view of the same spectra (b), and gain/phase plots (c, d) plots acquired from $(La_{0.8}Sr_{0.2})_{0.95}MnO_{3+\delta}$ microelectrodes. Specific parameters for these spectra: Library #1, 200 μm diameter, 192 nm thickness, measured at ~710 °C over the frequency range 10 kHz - 32 mHz. For the 1 atm O_2 data, the results from a full 7-parameter fit to Equation 1 (dashed red line) and a 6-parameter fit holding R_{ion} fixed (solid black line) are shown; they fall so closely on top of each other in these plots as to be indistinguishable.

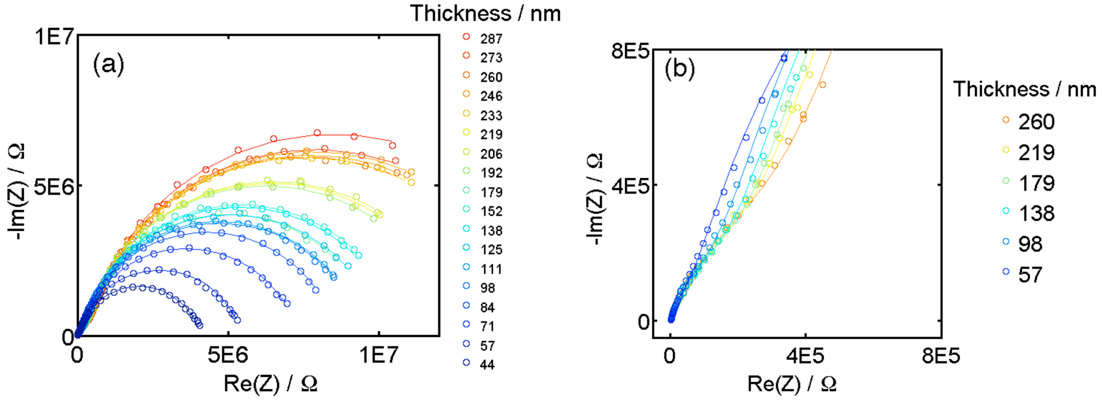

Figure 2.10. (a) Impedance spectra measured at ~710 ˚C and 0.01 atm O_2 from $La_{0.8}Sr_{0.2})_{0.95}MnO_{3+\delta}$ microelectrodes of various thicknesses in Library #1. (b) Zoomed view of a subset of the same spectra.

The exponent parameter of the constant phase element used to model the surface ionic capacitance was found to be ~0.7 and exhibited no trend with thickness or diameter (Figure S8). The diameter dependence of the other six fit parameters acquired from microelectrodes in the thickness library is shown in Figure 2.11. Considering first the parameter R_0, Figure 2.11e, it is seen to scale approximately linearly with the inverse of the microelectrode diameter (log-log slope of -1), as expected if R_0 corresponds primarily to bulk diffusion of oxygen ions from a small working electrode through a (solid) electrolyte to a large counter electrode.[28] The slopes are actually slightly steeper than -1; this is attributed to the tip cooling effect discussed in the Supplemental Information. From the expression $\sigma = 1/(2dR_0)$, where d is the microelectrode diameter, the oxygen ion conductivity σ of the YSZ was estimated and found to be in reasonable agreement with the actual value.

The three capacitance parameters are seen to scale with the square of diameter, while the two other resistances scale approximately with the inverse square of diameter. This scaling behavior was observed previously[10] and is consistent with the electrochemical pathway posited above, in which surface exchange occurs over the entire LSM surface and oxygen ion diffusion occurs primarily through the film. In contrast, a pathway mediated by the triple-phase-boundary (where the LSM, YSZ, and gas phases intersect) at the edge of the LSM would be expected to exhibit different scaling behavior.

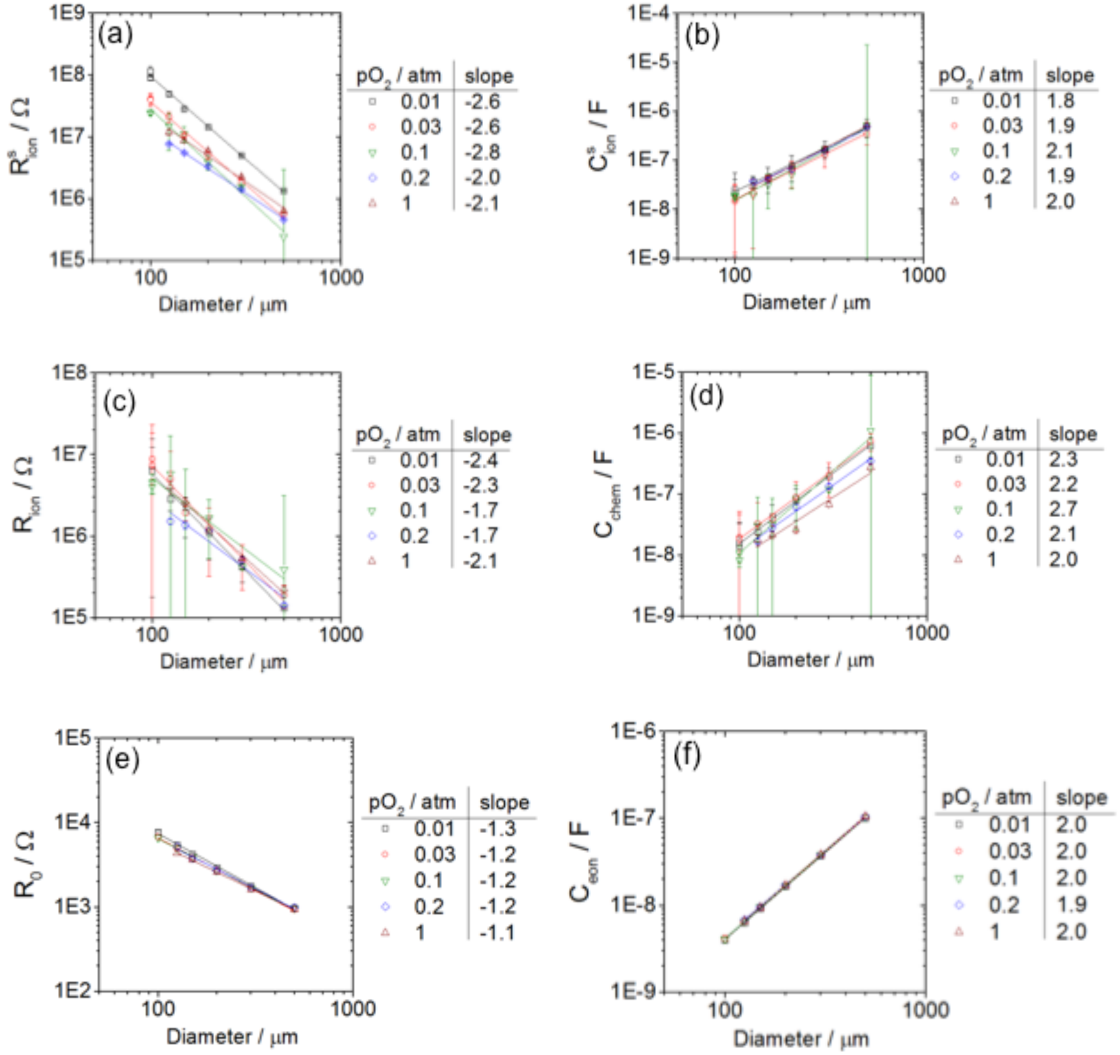

Figure 2.11. Diameter dependence of the six fit parameters measured from a thickness library of (La$_{0.8}$Sr$_{0.2}$)$_{0.95}$MnO$_{3+\delta}$ films (Library #1) at ~710 ˚C under various oxygen partial pressures with 246 nm microelectrode thickness. The lines are linear fits, the slopes of which are indicated next to the legend. 95% confidence intervals from the fits are shown, except where they are smaller than the data points.

Further validation of the electrochemical model can be obtained by considering the thickness dependence of the fit parameters. In a preliminary set of fits, all seven parameters were allowed to vary, however the results obtained for R_{ion} and C_{chem} were unreasonably scattered at 0.2 atm and 1 atm (Figure S25). This increased scatter was also observed by other workers at ~800 ˚C, and it can be attributed to the increased overlap of the lower and higher frequency arcs.[10] In other words, the characteristic frequencies of the surface exchange and bulk diffusion processes are close enough at 0.2 atm and 1 atm that the processes begin to be difficult to decouple by impedance spectroscopy. However, at the other pressures R_{ion} was seen to be insensitive to pO2 (Figure S25), so taking advantage of this insensitivity, the fits at 1 atm O_2 and 0.2 atm O_2 were performed using a value of R_{ion} fixed at the average R_{ion} obtained for the same microelectrode at the lower oxygen pressures (0.01 atm, 0.03 atm, and 0.1 atm). The results are shown in Figure 2.12.

The fit results are physically reasonable. C_{eon} is seen to be essentially independent of thickness, as expected for an interfacial quantity. R_0 is largely independent of thickness, also as expected; the slight increase in R_0 for the thinnest films is attributed to a small contribution from electronic sheet resistance. This sheet resistance is expected to have a negligible impact on the other fit parameters, because those parameters correspond to processes whose characteristic frequencies are orders of magnitude slower.[15] R_{ion} and C_{chem} are also seen to scale linearly with thickness, as expected since these parameters correspond to the diffusion resistance through the film and the film's bulk chemical capacitance. The ambipolar diffusivity can be calculated from the expression $D_{chem} = L^2/(R_{ion}*C_{chem})$.[26] The calculated values were found to be nearly independent of thickness (Figure S26), so the values were averaged over all thicknesses. As shown in Figure 2.13a, the resulting values for D_{chem} are consistent with the range of values measured from $La_{0.8}Sr_{0.2}MnO_{3+\delta}$ bulk samples in a previous study.[29] This consistency provides further validation of the electrochemical model used in this study.

The volume-normalized chemical capacitance can be found from the slope of each isobaric linear fit in Figure 2.12d; this result is plotted in Figure 2.13b along with comparable values reported for bulk samples of $La_{0.8}Sr_{0.2}MnO_{3+\delta}$ and thin film samples of $(La_{0.8}Sr_{0.2})_{0.92}MnO_{3+\delta}$. The temperatures and compositions in this comparison are not identical, but nevertheless there is a strong indication that the chemical capacitance under the conditions studied is almost two orders of magnitude lower in the thin films than in bulk samples. In other words, the redox thermodynamics of LSM appear to be different in these films compared to bulk samples; the films are less easily reducible.

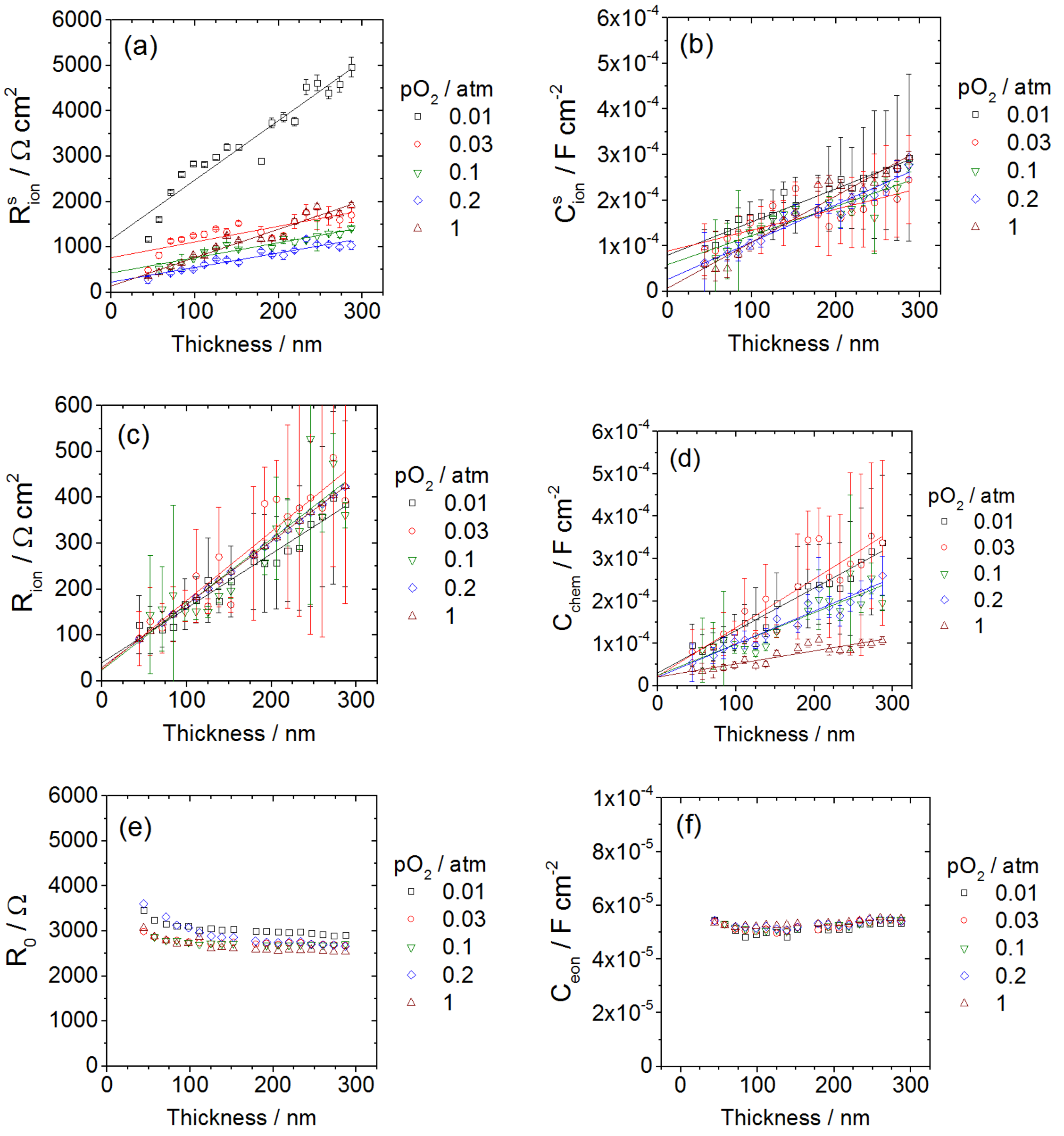

Figure 2.12. Thickness dependence of the six fit parameters measured from a thickness library of $(La_{0.8}Sr_{0.2})_{0.95}MnO_{3+\delta}$ films, Library #1, at ~710 ˚C and the indicated oxygen partial pressures. When fitting the spectra acquired under 0.2 atm O_2 and 1 atm O_2, R_{ion} was held fixed at the value determined by averaging the R_{ion} values obtained from the fits to impedance spectra acquired from the same microelectrode at 0.01 atm O_2, 0.03 atm O_2, and 0.1 atm O_2. 95% confidence intervals for the fits are shown, except where they are smaller than the data points.

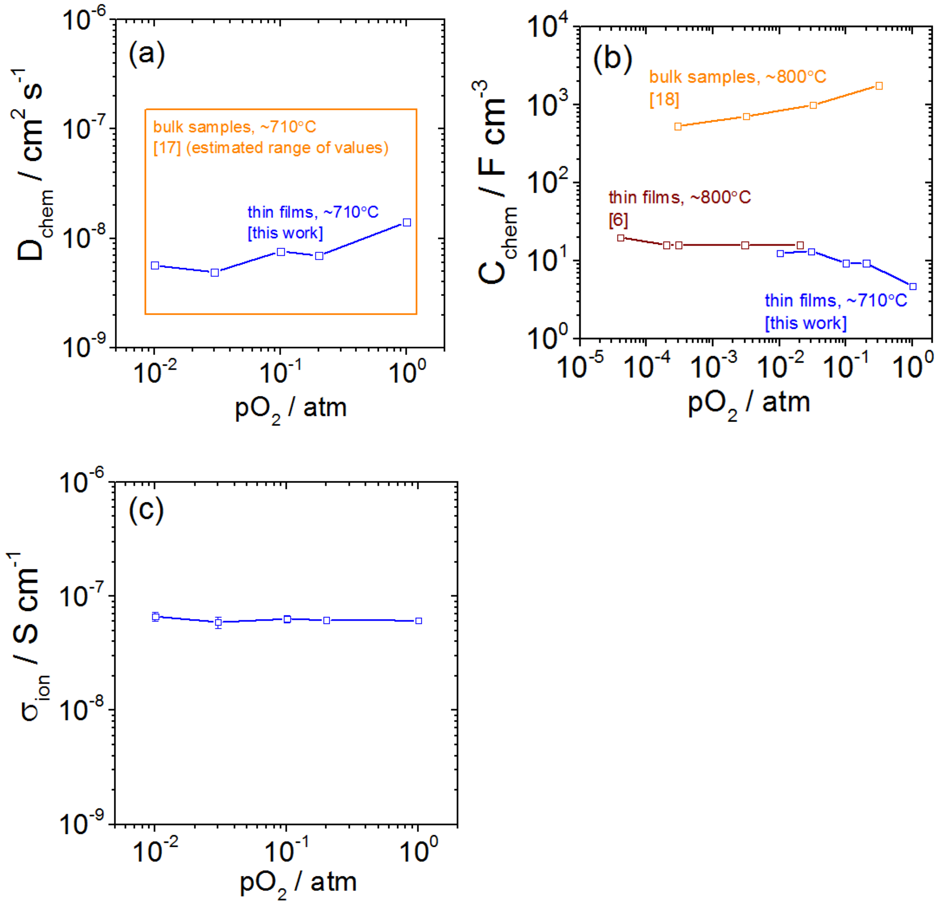

Figure 2.13. Ambipolar diffusivity D_{chem} (left) and volume-normalized chemical capacitance C_{chem} (right) of $(La_{0.8}Sr_{0.2})_{0.95}MnO_{3+\delta}$ at ~710 °C. The orange box bounds the range of values for D_{chem} previously measured from bulk samples of $La_{0.8}Sr_{0.2}MnO_{3+\delta}$.[29] Comparable literature data is also shown for C_{chem}.[10,30]

Returning to the surface parameters in Figure 2.12, it is striking that the parameters R_{ion}^{s} and C_{ion}^{s} --- which represent the surface exchange resistance and the effective surface ionic capacitance --- exhibit a linear dependence on thickness. Apparently the surface is somehow changing with thickness in a way that impacts the surface exchange rate. Since the area density of grain boundaries at the surface is observed to decrease with increasing thickness (Figure 2.4), one can hypothesize that surface grain boundaries are more active than surface grains in these LSM films.

The growth temperature library, Library #3, provides an excellent test for this hypothesis, since in that library the surface density of grain boundaries varies substantially while the thickness is uniform. Impedance spectra acquired from that library are shown in Figure 2.14. Again a large arc is observed at lower frequencies, and an additional smaller arc is observed at higher frequencies. Both arcs increase in magnitude with increasing growth temperature.

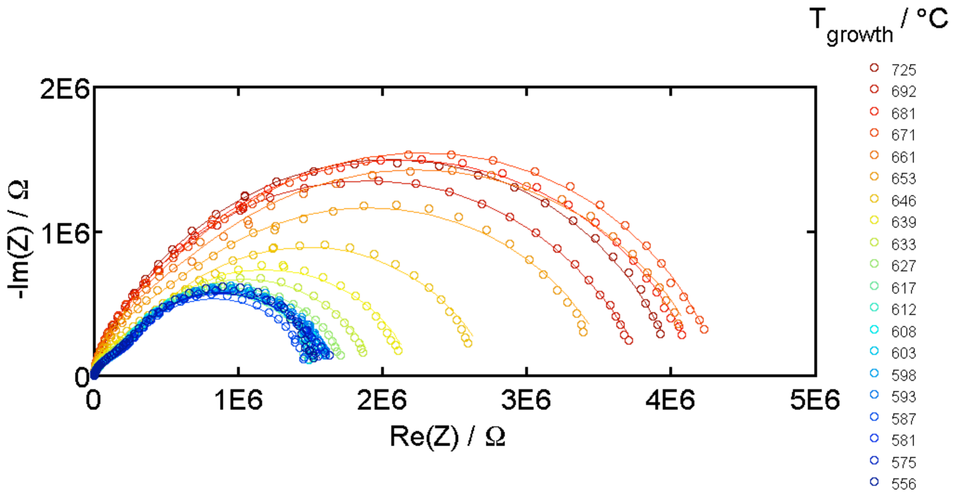

Figure 2.14. Impedance spectra acquired from the temperature-gradient $(La_{0.8}Sr_{0.2})_{0.95}MnO_{3+\delta}$ library under 0.2 atm O_2, ~710 ˚C, 200 μm diameter electrodes, over the frequency range 10 kHz - 32 mHz. Points are raw data, curves are fits to Equation 1.

Circuit parameters extracted from fitting these spectra are shown in Figure 2.15. The surface exchange resistance R_{ion}^{s} tends to increase with increasing growth temperature, while the surface ionic capacitance C_{ion}^{s} tends to decrease, and the changes predominantly occur in the growth temperature range 630 - 680 ˚C, a range in which the grain size also increases substantially (Figure 2.5).

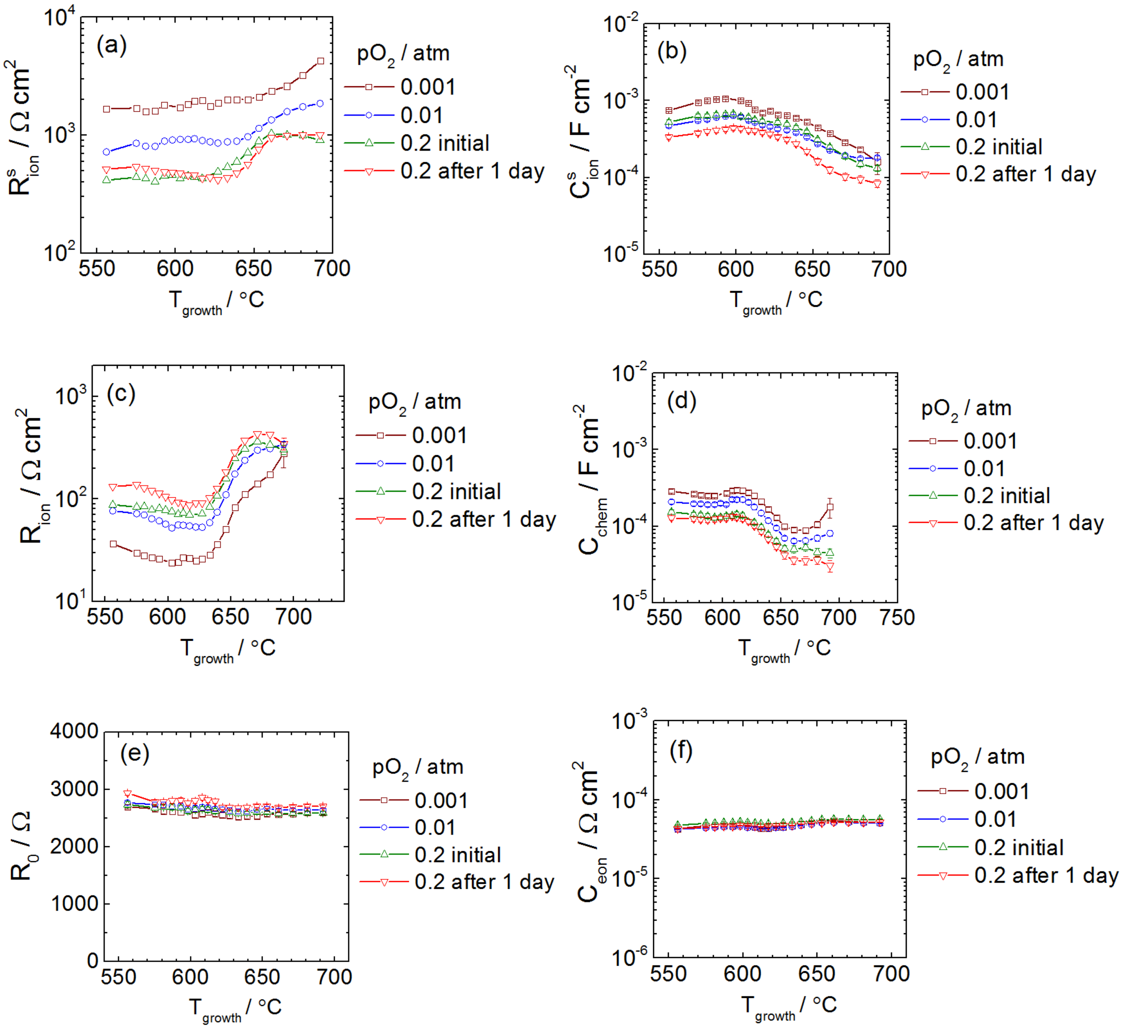

Figure 2.15. Fit parameters measured from the growth temperature library of $(La_{0.8}Sr_{0.2})_{0.95}MnO_{3+\delta}$ films, Library #3, at ~710 °C and the indicated pO2. The microelectrode dimensions were 200 µm diameter and 135 nm thickness throughout. Lines connect the points as guides for the eye. 95% confidence intervals are shown, except where they are smaller than the data points.

To explore this correlation, the area density of grain boundary length on the film surfaces can be estimated from image analyses of AFM micrographs. Figure S27 shows an example of a processed image, and the extracted values are plotted as a function of growth temperature or thickness in Figure S28. The inverse of the LSM surface exchange resistance (which is a direct measure of surface activity) can then be plotted as a function of the area density of grain boundary length. The results are shown in Figure 2.16. For each library, the surface activity is seen to scale linearly with the area density of grain boundary length, indicating that the grain boundaries are more catalytically active than the grain surfaces. From the slopes of these trends, it can be estimated that the surface activity of an LSM film increases by $10^{-13}\ \Omega^{-1}$ per micron of added grain boundary length.

It is also notable that R_{ion} tends to increase and C_{chem} tends to decrease with increasing growth temperature (area density of grain boundary length). These trends suggest that the oxygen ion diffusivity may be higher along grain boundaries than through grains. This suggestion is consistent with previous work on bulk samples, in which SIMS measurements of oxygen tracer diffusion in $La_{0.8}Sr_{0.2}MnO_{3+\delta}$ found evidence of short circuit diffusion that was ascribed to fast diffusion along grain boundaries.[31] However, despite the small confidence intervals obtained in these fits, we cannot entirely rule out the possibility that the R_{ion} and C_{chem} trends with growth temperature are fitting artifacts that arise from the increased overlap in characteristic frequencies of the surface and bulk processes.

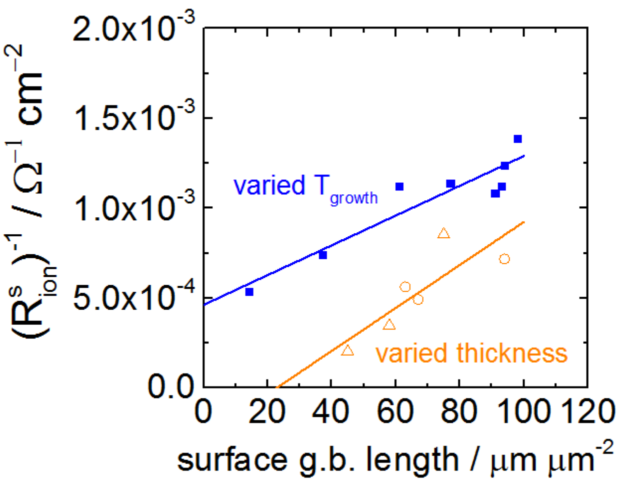

Figure 2.16. Electrochemical activity measured at ~710 ˚C under 0.01 atm O_2 from libraries of $(La_{0.8}Sr_{0.2})_{0.95}MnO_{3+\delta}$ microelectrodes with 200 µm diameter and various growth temperature (blue squares, 10 mtorr O_2 growth) or various thicknesses (orange, triangles and circles are samples grown in 30 mtorr O_2 and 10 mtorr O_2, respectively).

2.6 Discussion

The finding that grain boundaries are correlated with improved surface activity of LSM films explains how the low frequency arc can correspond to the surface exchange process and simultaneously grow with increasing thickness. It also indicates that ion transport through such films is less limiting than many reports previously suggested.

An additional implication is that patterning LSM films by wet etching may lead to different results than patterning films by dry etching. Wet etchants typically undercut the photoresist, such that at each etched edge, the film thickness tapers to zero over a tapered region that is roughly 10 μm wide.[23] This tapered region may comprise a significant fraction of the total area, e.g., for a 100 μm circular microelectrode, a tapered edge region of width 10 μm would span roughly one third of the total surface area and, based on the results presented above, the tapered region could have a higher density of exposed grain boundaries and a higher surface activity. A second enhancement may arise because electrodes produced by wet etching are effectively acid etched in the tapered edge region, and acid etching has been observed to significantly improve the activity of MIEC electrodes made of materials like LSM and LSC.[32,33] These enhancements were avoided in the current study by patterning the films using dry etching (argon ion milling), which yielded a sharper edge with no acid exposure (Figure S30).

Returning to Figure 2.16, it is apparent that although the trends of activity with exposed grain boundary length are similar between the two types of libraries, the trends have different intercepts, such that the absolute magnitude of the surface activity is different by approximately a factor of 2. The origin of this performance difference between the two types of libraries is unclear. Comparable batch-to-batch performance variations have sometimes been observed in previous studies of films grown by pulsed laser deposition.[34] To help pin down the origin of this factor of 2, a second thickness library was grown under 30 mtorr O_2 pressure, patterned, and then characterized. The results from this library are plotted in Figure 2.16 and Figure S31 and are quite similar to the thickness library grown under 10 mtorr O_2, indicating that small differences in oxygen partial pressure during growth are unlikely to be the origin of the factor of 2. The microelectrodes in this second thickness library also exhibited stable surface activity over the ~50 h time period in which the measurements were acquired (Figure S31) so the factor of 2 does not appear to originate from non-stationary behavior of the surfaces during the impedance measurements. It is notable that the growth temperature library was grown with an ablation laser pulse rate of 5 Hz, while the thickness libraries used 1 Hz. One can speculate that the faster growth rate led to the higher surface activity, perhaps by influencing the extent to which cations and impurities were able to segregate to the surface during growth.

2.7 Conclusion

A scanning impedance probe was developed that can measure the electrochemical impedance response of hundreds of thin film microelectrodes in automated fashion. This instrument was used to characterize libraries of LSM microelectrodes with systematically varied diameter and either thickness or growth temperature. The electrochemical impedance response of all microelectrodes at ~710 °C was found to be well fit by a physically derived equivalent circuit, and all trends were consistent with a pathway involving oxygen reduction over the entire surface of the LSM microelectrode followed by diffusion through the film and into the YSZ electrolyte. The surface activity was found to scale linearly with the area density of grain boundary length on the LSM microelectrode surface, suggesting that grain boundaries are more active than grains towards the rate-limiting surface step. This finding suggests that increasing the area density of exposed grain boundary length in a practical LSM-based electrode could lead to substantial improvements in activity.

Chapter 2 Supplemental Information

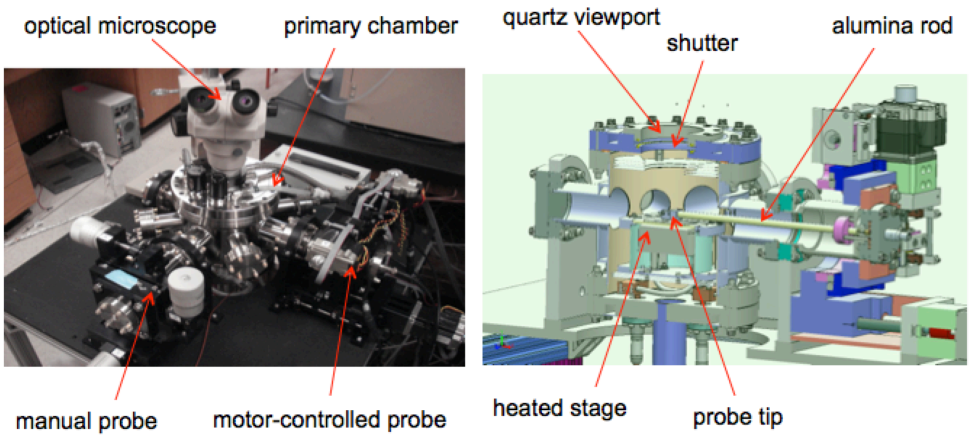

Figure S17. Primary chamber of the scanning impedance probe. Left: external photo. Right: computer model cross-section showing the chamber interior.

Figure S18. Optical photo of the stage used to asymmetrically heat substrates during preparation of the library of growth temperatures.

Temperature calibration

The samples were heated from below, so the metal probe tip was cooler than the sample and thus the probe tip cooled the microelectrode by conduction during each impedance measurement. The smaller the microelectrode diameter, the more the average microelectrode temperature is expected to be lowered by tip cooling. This effect was first reported by Opitz and Fleig in 2010;[35] it appears to have been neglected in many reports using microelectrodes published before then.

Opitz and Fleig also observed that the associated temperature drop between the counter electrode and the microelectrode generates a measurable Seebeck voltage.[35] From this temperature drop across the substrate and the substrate Seebeck coefficient (~0.5 mV/K for YSZ[36]), the actual average microelectrode temperature can be estimated. Typical results measured in the current work are shown Figure S19. It is noteworthy that the cooling is not instantaneous; rather, the thermovoltage typically took 5 s - 180 s to stabilize, with the faster times corresponding to the higher temperatures or larger diameters. The observed thermovoltage also varied slightly between measurements, and larger thermovoltages were observed when contacting metal microelectrodes than when contacting the oxide microelectrodes used in this study. These effects are likely both explained by differences in thermomechanical contact and thermal conductivity at the contact point. In addition, besides the temperature drop between the electrodes, there is an additional small temperature drop between the heated stage surface and the sample counter electrode. This drop was measured separately using representative substrates and thin thermocouples.

In summary, with a stage temperature setpoint of 750 ˚C the average actual temperature of the microelectrodes under test was estimated as ranging from ~700 ˚C (for 100 µm diameter) up to ~720 ˚C (for 500 µm diameter).

In Figure 2.11 the deviations in the log-log relationships from the expected slope of -2.0 are attributed primarily to the temperature effects described above. Note that this tip cooling effect is not expected to significantly distort any of the other impedance trends reported in this work, since apart from Figure 2.11 only microelectrodes with 200 µm diameter were measured.

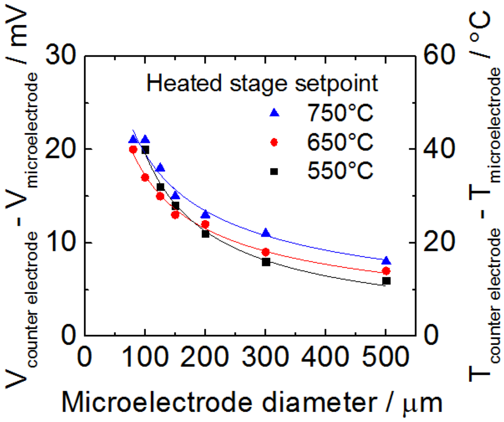

Figure S19. Seebeck voltage measured between the counter electrode and an oxide microelectrode contacted by a Paliney7 probe tip. Rescaling the voltage by the Seebeck coefficient of YSZ yields an estimate for the associated temperature drop between the electrodes, also shown. Curves are power-law fits to the data at each temperature.

Sources of uncertainty in tip position

The total tolerance in tip position that the scanning impedance probe can achieve includes several contributions with the following estimated magnitudes: the photolithography method used to pattern the films (±5 μm); the manual process of visually identifying reference points (±10 μm); the stepper motor positioning accuracy (±1 μm); creep of the Paliney7 probe tip at high temperatures (±10 μm); deflection of the tip due to contact forces with the substrate (±10 μm). The resulting total tolerance in tip position motivated the use of microelectrodes with sufficiently large diameter (≥ 100 μm) so as to ensure that reliable electrical contact could be achieved throughout the study. $Pt_{0.7}Ir_{0.3}$ probe tips exhibited reduced creep and deflection but typically scratched the films at elevated temperature. By reducing the above tolerances it should be possible in future studies to reliably contact microelectrodes with smaller diameters.

Fitting routine: Choosing the initial values

Depending on the initial values chosen for the fit parameters, the fitting routine sometimes either failed to converge or converged to a solution with unreasonably large confidence intervals for all parameters. It was found that these convergence problems could mostly be avoided by taking as the initial value of each fit parameter the median result for that parameter from preliminary fits to the same spectra that were performed using plausible but otherwise somewhat arbitrary initial values.

Additional Figures

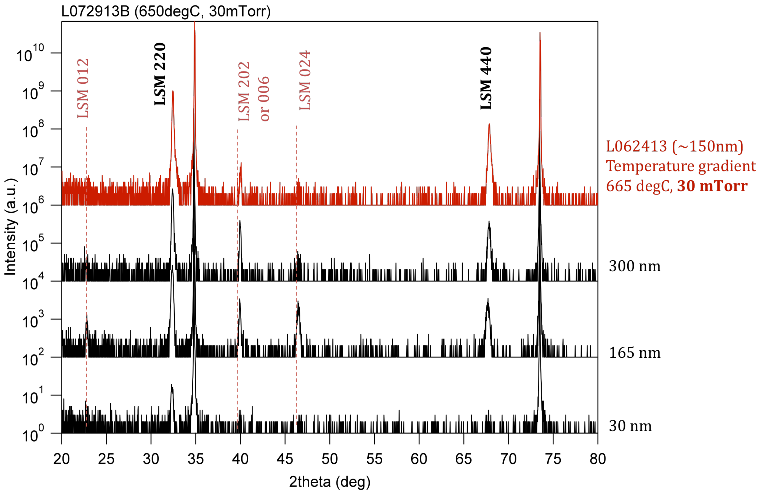

Figure S20. XRD patterns acquired from a thickness library of $(La_{0.8}Sr_{0.2})_{0.95}MnO_{3+\delta}$ microelectrodes, Library #2, grown at 650 ˚C under 10 mtorr O_2. The corresponding film thickness is listed to the right of each pattern. The orientation of each LSM reflection is also indicated. Reflections marked with an asterisk are from the YSZ substrate.

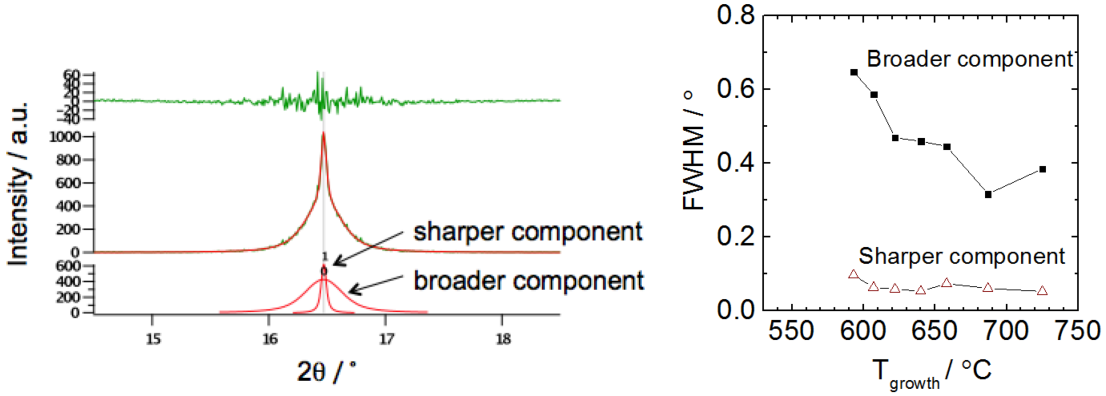

Figure S21. Left: Typical rocking curve acquired from the $(La_{0.8}Sr_{0.2})_{0.95}MnO_{3+\delta}$ growth temperature library in a region where T_{growth} = 725 °C. The two fit components are shown in red at bottom; the fit residual is shown in green at top. Right: Full width at half maximum (FWHM) values extracted from the rocking curves.

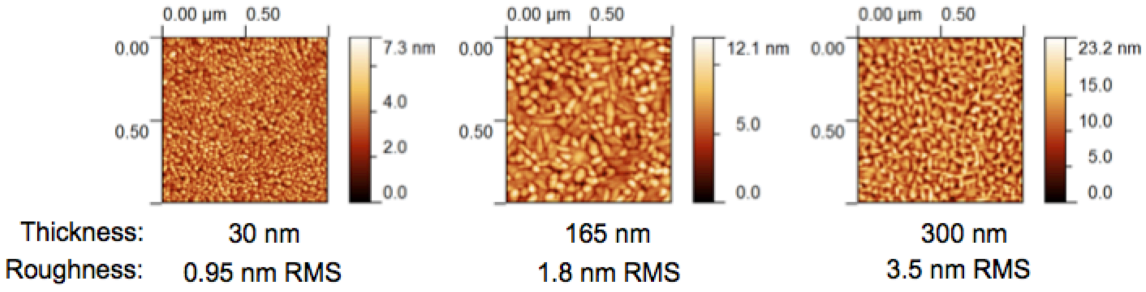

Figure S22. AFM images acquired after patterning from a follow-up thickness library of $(La_{0.8}Sr_{0.2})_{0.95}MnO_{3+\delta}$ microelectrodes grown at 650 °C under 10 mtorr O_2. The corresponding film thickness and root-mean-squared roughness are listed under each micrograph.

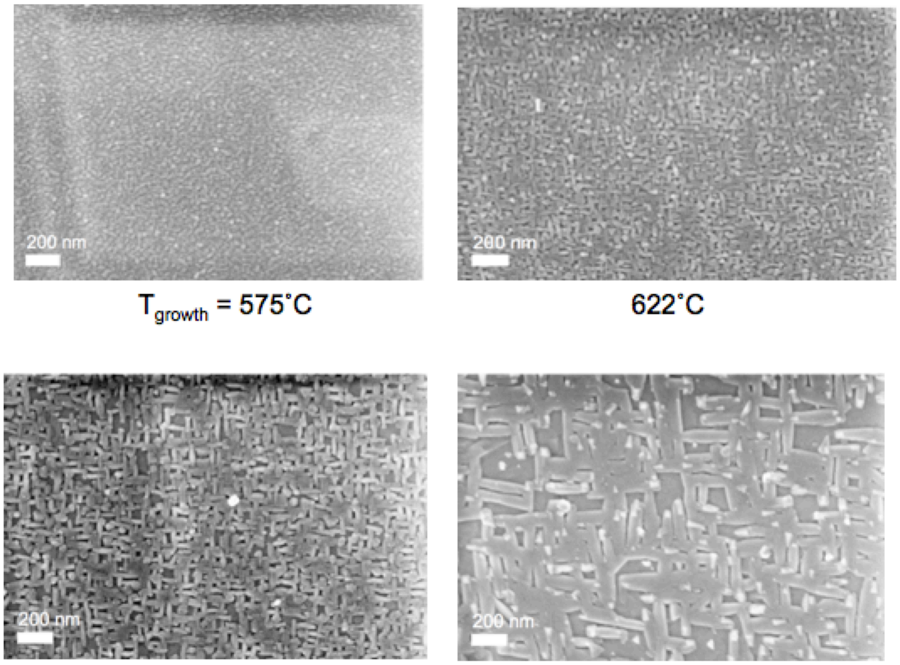

T_{growth} = 575°C

622°C

646°C

692°C

Figure S23. SEM images from the $(La_{0.8}Sr_{0.2})_{0.95}MnO_{3+\delta}$ growth temperature library after exposure for 2 days at ~710 °C in the scanning impedance probe. Some of the observed contrast is due to mild sample charging.

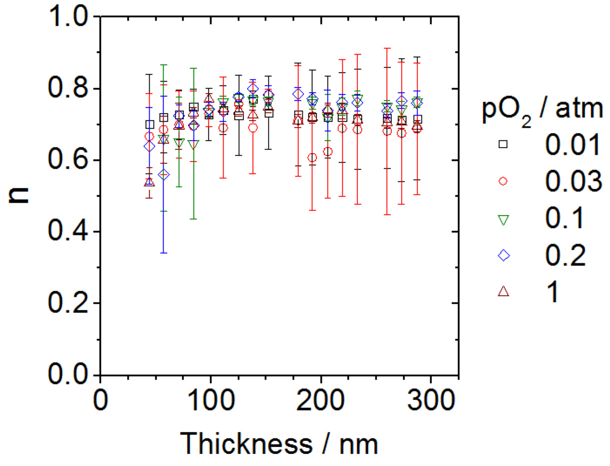

Figure S24. Exponent of the constant phase element used to represent the surface capacitance (C_{ion}^s) when fitting impedance spectra acquired from the thickness library at ~710 ˚C, 200 μm diameter to the model shown in Equation 1. 95% confidence intervals are shown.

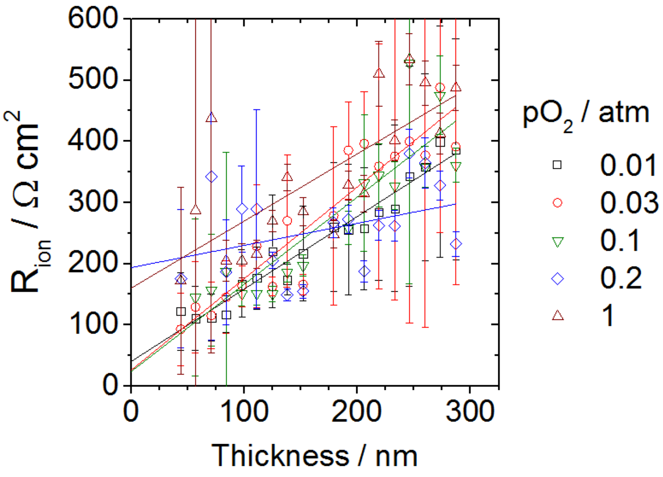

Figure S25. Thickness dependence of the fit parameter R_{ion} measured from the $(La_{0.8}Sr_{0.2})_{0.95}MnO_{3+\delta}$ thickness library at ~710 ˚C at various oxygen partial pressures. This plot is identical to the plot of R_{ion} in Figure 2.12, except here all seven parameters were free to vary in all fits, including the 0.2 atm and 1 atm fits. 95% confidence intervals are shown.

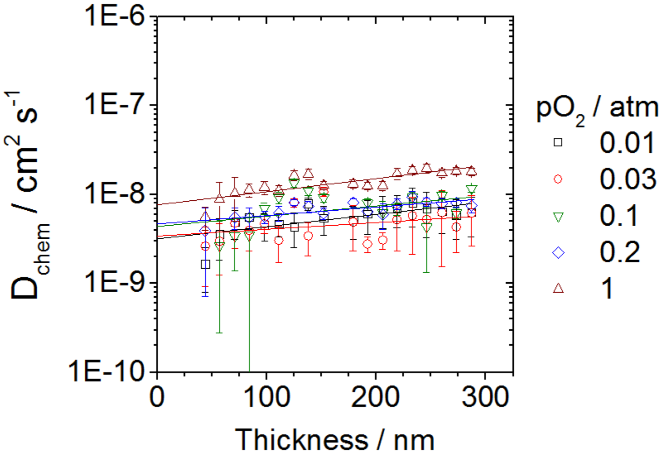

Figure S26. Thickness dependence of the ambipolar diffusivity D_{chem} calculated from the $(La_{0.8}Sr_{0.2})_{0.95}MnO_{3+\delta}$ thickness trends shown in Figure 2.12 for ~710 ˚C. 95% confidence intervals are shown. (They are artificially small for the 0.2 atm and 1 atm isobars, since R_{ion} was held fixed in those fits.)

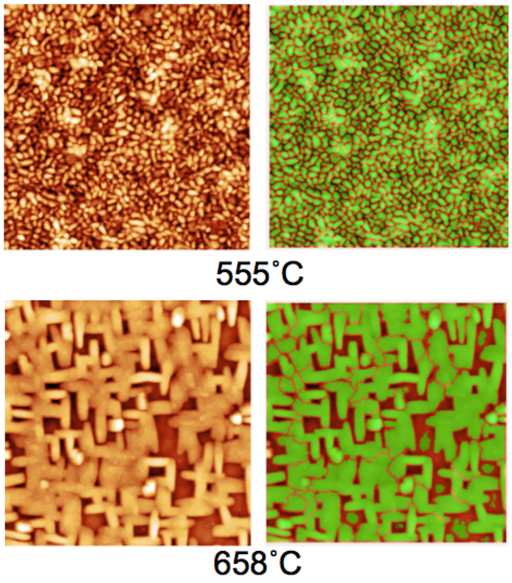

Figure S27. Typical images used to estimate the surface grain boundary length. Films grown at two different temperatures are shown. Left: AFM micrographs. Right: Same micrographs after image processing. The surface grain boundary length was estimated by summing the length of the borders between the green regions.

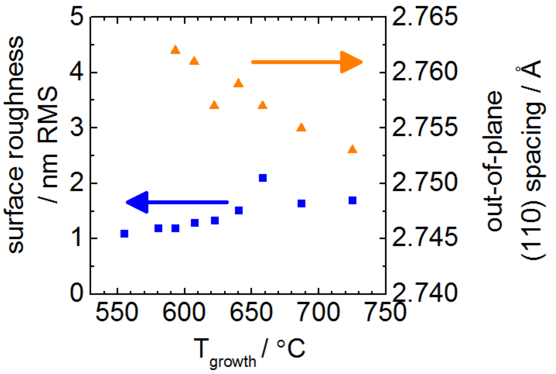

Figure S28. Surface roughness and out-of-plane (110) plane spacing measured from the as-grown $(La_{0.8}Sr_{0.2})_{0.95}MnO_{3+\delta}$ temperature library using AFM, XRD, and AFM, respectively.

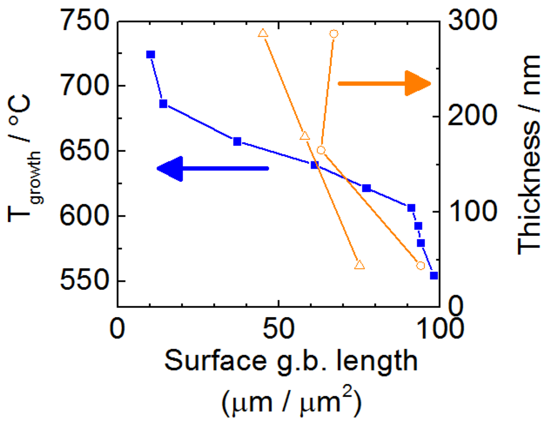

Figure S29. Surface grain boundary length estimated using AFM images from the growth temperature library (blue) and two thickness libraries grown at 10 mtorr O_2 (circles) and 30 mtorr O_2 (triangles).

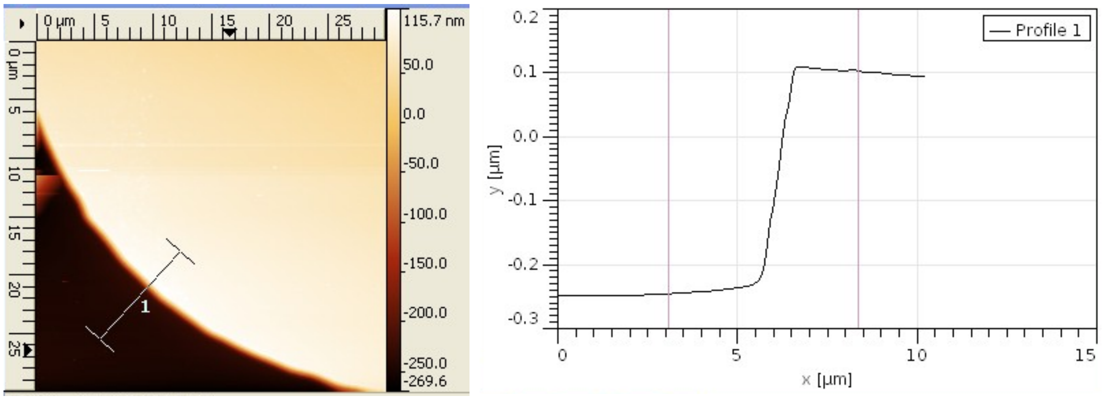

Figure S30. Example edge profile of an LSM microelectrode prepared by dry etching. This particular profile was acquired from an 80 µm diameter microelectrode in Library #1.

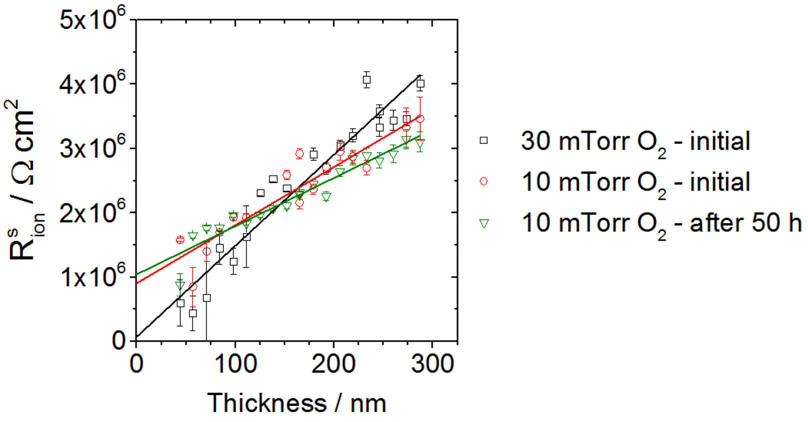

Figure S31. Surface resistance R_{ion}^s extracted from impedance spectra at 710 ˚C in 0.2 atm O_2 using 200 μm diameter microelectrodes from two thickness-gradient libraries grown on different substrates and measured separately. 95% confidence intervals are shown. Lines are linear fits.